Published in final edited form as:
IEEE Trans Med Imaging. 2011 May ; 30(5): 1090–1099. doi:10.1109/TMI.2010.2089519.

Compressed Sensing with Wavelet Domain Dependencies for Coronary MRI: A Retrospective Study

Mehmet Akçakaya, **Seunghoon Nam**, **Peng Hu**, **Mehdi H. Moghari**, **Long H. Ngo**, **Vahid Tarokh**, **Warren J. Manning**, and **Reza Nezafat**

M. Akçakaya and S. Nam are with the School of Engineering and Applied Sciences, Harvard University, Cambridge, MA, and with the Department of Medicine, Beth Israel Deaconess Medical Center, Harvard Medical School, Boston, MA. W. J. Manning is with the Department of Medicine and Department of Radiology, Beth Israel Deaconess Medical Center, Harvard Medical School, Boston, MA. V. Tarokh is with the School of Engineering and Applied Sciences, Harvard University, Cambridge, MA. P. Hu, M. H. Moghari, L. H. Ngo and R. Nezafat are with the Department of Medicine, Beth Israel Deaconess Medical Center, Harvard Medical School, Boston, MA

Mehmet Akçakaya: makcakay@bidmc.harvard.edu; Seunghoon Nam: snaml@bidmc.harvard.edu; Peng Hu: phul@bidmc.harvard.edu; Mehdi H. Moghari: mhedjazi@bidmc.harvard.edu; Long H. Ngo: lngo@bidmc.harvard.edu; Vahid Tarokh: vahid@seas.harvard.edu; Warren J. Manning: wmanning@bidmc.harvard.edu; Reza Nezafat: mezafat@bidmc.harvard.edu

Abstract

Coronary MRI is a non-invasive imaging modality for diagnosis of coronary artery disease. One of the limitations of coronary MRI is its long acquisition time due to the need of imaging with high spatial resolution and constraints on respiratory and cardiac motions. Compressed sensing (CS) has been recently utilized to accelerate image acquisition in MRI. In this paper, we develop an improved CS reconstruction method, Bayesian Least Squares – Gaussian Scale Mixture (BLS-GSM), that uses dependencies of wavelet domain coefficients to reduce the observed blurring and reconstruction artifacts in coronary MRI using traditional ℓ_1 regularization. Images of left and right coronary MRI was acquired in 7 healthy subjects with fully-sampled k-space data. The data was retrospectively undersampled using acceleration rates of 2, 4, 6 and 8 and reconstructed using ℓ_1 thresholding, ℓ_1 minimization and BLS-GSM thresholding. Reconstructed right and left coronary images were compared with fully-sampled reconstructions in vessel sharpness and subjective image quality (1–4 for poor-excellent). Mean square error (MSE) was also calculated for each reconstruction. There were no significant differences between the fully sampled image score vs. rate 2, 4 or 6 for BLS-GSM for both right and left coronaries (p = N.S.). However, for ℓ_1 thresholding significant differences ($p < 0.05$) were observed for rates higher than 2 and 4 for right and left coronaries respectively. ℓ_1 minimization also yields images with lower scores compared to the reference for rates higher than 4 for both coronaries. These results were consistent with the quantitative vessel sharpness readings. BLS-GSM allows acceleration of coronary MRI with acceleration rates beyond what can be achieved with ℓ_1 regularization.

Index Terms

Compressed sensing; wavelet domain dependencies; magnetic resonance imaging; coronary MRI; accelerated imaging; coronary artery disease

I. INTRODUCTION

Coronary artery disease (CAD) caused approximately 1 of every 6 deaths in the United States in 2006 [26]. In 2010, an estimated 785,000 Americans will have a new coronary attack, and approximately 470,000 will have a recurrent attack. Catheter based, diagnostic invasive x-ray coronary angiography remains the clinical "gold standard" for the diagnosis of significant (> 50% diameter stenosis) CAD with over a million catheter based x-ray coronary angiograms performed annually in the United States. Although numerous non-invasive tests are available to help discriminate among those with and without significant angiographic disease, up to 35% of patients referred for their initial elective catheter based x-ray coronary angiography are found to have no significant stenosis. Therefore, a non-invasive imaging alternative to diagnostic x-ray angiography is desirable.

Alternatives for non-invasive coronary artery imaging include multidetector computed tomography (MDCT) and magnetic resonance imaging (MRI). Advantages of coronary MDCT include rapid image acquisition as well as superior isotropic spatial resolution. Advantages of coronary MRI include the lack of ionizing radiation or need for iodinated contrast (thereby facilitating repeated or follow-up scanning) and smaller artifacts related to epicardial calcium. Despite considerable advances in the past decade in coronary MRI, long data acquisition time of coronary MRI has been one of the main limitations of this technique. Several approaches such as partial Fourier, non-Cartesian sampling [29], [30], parallel imaging [20], [31], [32], [35], [40], use of exogenous contrast with efficient sampling [3], [4] have been used to accelerate image acquisition in coronary MRI. With all these efforts, the acquisition time for coronary MRI still remains long (5–10 min). Therefore, developments of methods to reduce data acquisition time in coronary MRI are appealing.

Compressed (or compressive) sensing (CS) is a novel approach that allows reconstruction of an image from a partially sampled k-space data [5], [27]. CS exploits the sparsity (or more generally the compressibility) of the image in a transform domain to reduce the required minimal data for reconstruction of an artifact-free image. CS reconstruction aims to minimize the sparsity of the reconstructed image in a transform domain subject to data consistency constraints comparing the estimate to the acquired k-space data. Minimization of the number of non-zero coefficients, which is a direct measure of sparsity, is NP-hard in general. Thus alternative measures, such as the ℓ_1 norm of the transform domain coefficients have been used instead [7], [14].

There have been recent investigations of feasibility of CS in improving the imaging contrast in non-contrast enhanced steady-state free precession (SSFP) angiography [11], accelerating image acquisition in dynamic MRI [19] and first-pass cardiac perfusion MRI [33], and three-dimensional imaging of upper airways [23]. In all these studies, the reconstruction

method has been based on minimizing an ℓ_1 objective function. This objective function results in blurring of the vessel boundaries that could limit its use in high resolution coronary imaging.

In this study, we sought to develop and investigate an improved CS reconstruction method that uses the dependencies of the wavelet domain coefficients and demonstrate its utility in accelerating coronary MRI data acquisition.

II. THEORY

A. Compressed Sensing via ℓ_p regularization

Let $\mathbf{m}$ be the imaging data of size $n_1 \times n_2 \times n_3$ and $\mathbf{F}$ be the Fourier transform. Let $\mathbf{F}_\Omega$ denote the undersampling operator that keeps a subset Ω of the k-space and rearranges it to a vector, where $|\Omega| < n_1 \cdot n_2 \cdot n_3$. When the k-space is undersampled using the sampling pattern Ω, the measurement in the j^{th} coil is given by

$$\mathbf{s_j} = \mathbf{F}_\Omega(C_j \mathbf{m}) + \mathbf{n_j},$$

where C_j is the coil sensitivity map of the j^{th} coil and $\mathbf{n_j}$ is an additive noise vector.

Conventional CS reconstruction solves a minimization problem based on an objective function:

$$\hat{\mathbf{m}} = \arg\min_{\mathbf{m}} \|\mathbf{S} - \mathbf{F}_\Omega(\mathbf{m})\|_2^2 + \tau\Phi(\mathbf{\Psi m}), \quad (1)$$

where the first term is a fidelity measure of image consistency (i.e. the difference between the measured k-space data and the undersampled k-space of the estimated image) and the second term is a sparsity regularizer Φ with weight τ. Typically Φ is chosen as the (p^{th} power of) ℓ_p ($p \leq 1$) norm of transform domain coefficients (e.g. wavelet or finite differences), which captures the sparsity of the image in a transform domain $\mathbf{\Psi}$ [5], [9], [27], [43]. From a Bayesian perspective, this regularization can be expressed as a maximum a posteriori (MAP) estimation:

$$\begin{aligned} \hat{\mathbf{m}}_{\text{MAP}} &= \arg\max_{\mathbf{m}} \log p(\mathbf{m}|\mathbf{S}) \\ &= \arg\max_{\mathbf{m}} (\log p(\mathbf{S}|\mathbf{m}) + \log p(\mathbf{m})). \end{aligned} \quad (2)$$

In the presence of Gaussian measurement noise, the first term, $\log p(\mathbf{S}|\mathbf{m})$ corresponds to the data fidelity term in Equation (1). The second term, $\log p(\mathbf{m})$ corresponds to the weighted sparsity regularizer in Equation (1), and after appropriate scaling (with the noise variance) it can be shown to correspond to using $p(\mathbf{m}) \propto \exp(-\tau\Phi(\mathbf{\Psi m}))$ as the probability density function of the $\mathbf{\Psi}$-transform coefficients [17]. Thus, regularizers based on ℓ_p norms correspond to independent and identically distributed (i.i.d.) transform domain coefficients.

B. Modeling Wavelet Domain Sparsity and Dependencies

ℓ_p norm regularizers in CS reconstruction treat wavelet domain coefficients as independent variables without considering additional information from the neighboring coefficients.

However, there is correlation between the wavelet coefficients of a given neighborhood that includes surrounding coefficients from the same subband, as well as neighboring coefficients from nearby scales [34]. There is also dependency between parent and child wavelet coefficients [2], [38]. Figure 1a shows the Haar wavelet coefficients of a 2D slice of a coronary image, which shows that a large wavelet coefficient in a given subband is likely to have large wavelet coefficients surrounding it. If a random permutation is applied to these wavelet coefficients, this structure is lost, yet the ℓ_p norm is preserved. This suggests that an independent coefficient model for the wavelet transform may not be capturing optimal information about the MR images. In this study, we investigate if additional information about the dependencies of the wavelet coefficients can improve image reconstruction for coronary MRI. Therefore, we will use a Gaussian scale mixture (GSM) model that can simultaneously capture the correlation and the sparseness of the wavelet transform [34] for reconstruction of coronary MRI.

The wavelet transform ($\mathbf{\Psi}$) of an image **m** consists of coefficients $u_l^{s,o}$ where *o*, *s* and *l* specify the orientation of the subband, its scale and the location of the coefficient within the subband respectively. In the GSM model, the neighborhood of the wavelet transform coefficients (**x**) surrounding $u_l^{s,o}$ can be expressed as a zero-mean Gaussian vector $\boldsymbol{\theta}$ weighted by a scalar random variable *z* with Jeffrey's prior ($p_z(z) = 1/z$) [1], [34]:

$$\mathbf{x} = \sqrt{z}\boldsymbol{\theta},$$

where the sparsity is modeled by *z*, as discussed in Appendix A, and the correlation between the neighboring coefficients is modeled using the local covariance of the subband at scale *s* and orientation *o*, $\mathbf{C}_{\boldsymbol{\theta}}^{s,o}$ [34].

C. CS Image Reconstruction

Figure 2 shows the proposed coronary MRI reconstruction algorithm, which is based on the iterative soft thresholding (IST) algorithm [10], [12], [17]. It alternates between enforcing k-space data consistency and de-aliasing, as follows: The current image estimate ($\mathbf{m}^{(t)}$) is weighted by coil sensitivity map (C_k) of each individual coil elements. This B_1 weighted imaging data sets are then transformed to the Fourier space and in a data consistency step, the estimated k-space lines corresponding to the ones that were acquired during acquisition are replaced with the acquired k-space lines. The k-space data is then transformed into the image space using inverse Fourier transform and weighted by the conjugate of each individual coil maps and combined into a single image ($\mathbf{v}^{(t)}$). In the dealiasing stage, the estimated image ($\mathbf{v}^{(t)}$) is thresholded using the proposed Bayesian Least Squares (BLS)-GSM method [34] depicted in Figure 3.

In the first step of the BLS-GSM thresholding, the current aliased image estimate $\mathbf{v}^{(t)}$ is transformed to wavelet domain using a full steerable pyramids [34], [39] for complex data. The wavelet domain neighborhood **h** surrounding $u_l^{s,o}$ in the current aliased estimate is defined as a 3 × 3 neighborhood of $u_l^{s,o}$ in the same subband, and the parent wavelet coefficient from the adjacent subband. **h** is modeled as $\mathbf{h}=\mathbf{x}+\mathbf{w}=\sqrt{z}\boldsymbol{\theta}+\mathbf{w}$, by the

corresponding neighborhood **x** from the original unaliased image perturbed by a noise term **w** that only depends on the measurement noise **n** [17]. Each $u_l^{s,o}$ undergoes a thresholding step that results in a new estimate $u_l^{s,o-thr}$ according to:

$$u_l^{s,o-thr}=\mathbb{E}(u_l^{s,o}|\mathbf{h})=\int_0^\infty \mathbb{E}(u_l^{s,o}|\mathbf{h},z)p(z|\mathbf{h})dz. \quad (3)$$

where $\mathbb{E}$ is the expectation operator. This new estimate, $u_l^{s,o-thr}$, can be calculated numerically as described below.

As described in Section II-B, the wavelet dependencies are exhibited for neighboring coefficients in the same subband, and for parent-children wavelet coefficients, hence each subband is handled separately. First, the sample covariance $\mathbf{C}_\mathbf{h}^{s,o}$ for each subband of the wavelet transform of the current image estimate $\mathbf{v}^{(t)}$ is calculated, followed by the computation of noise covariance $\mathbf{C}_\mathbf{w}^{s,o}$ for the power spectral density corresponding to white Gaussian noise with mean 0 and variance 1 [34]. The neighborhood covariance $\mathbf{C}_{\boldsymbol{\theta}}^{s,o}$ is also estimated using the noise-compensated sample covariance matrix from the aliased data as $(\mathbf{C}_\mathbf{h}^{s,o}-\tau\mathbf{C}_\mathbf{w}^{s,o})_+$, where only the positive semi-definite part is preserved. For a given *z*, the first term in the integration can then be expressed as:

$$\mathbb{E}(\mathbf{x}|\mathbf{h},z)=z\mathbf{C}_{\boldsymbol{\theta}}^{s,o}(z\mathbf{C}_{\boldsymbol{\theta}}^{s,o}+\tau\mathbf{C}_\mathbf{w}^{s,o})^{-1}\mathbf{h},$$

which is the Wiener estimate, where the expectation is over the Gaussian noise **w**. For a given value of *z*, $p(\mathbf{h}|z)$ is a Gaussian probability density function with mean 0 and covariance matrix $z\mathbf{C}_{\boldsymbol{\theta}}^{s,o}+\tau\mathbf{C}_\mathbf{w}^{s,o}$. Hence, using the distribution of $p_z(z)$, $p(z|\mathbf{h})$ can be calculated via Bayes' rule numerically, for all *z* in the integration range [34]. The new thresholded estimate, $u_l^{s,o-thr}$ can then be calculated using the coordinate corresponding to the neighborhood center in the Wiener estimate vector (i.e. $\mathbb{E}(u_l^{s,o}|\mathbf{h},z)$), and $p(z|\mathbf{h})$ by numerical integration over *z*.

The $u_l^{s,o-thr}$ which are calculated for each neighborhood **h** are then replaced and a new image estimate is obtained using an inverse wavelet transform. The new estimated image is then used as an input to the CS data consistency algorithm outlined in Figure 2. The reconstruction method was iterated for 30 to 100 times based on acceleration rates, although empirical convergence of $\|\mathbf{m}^{(t)}-\mathbf{m}^{(t-1)}\|_2/\|\mathbf{m}^{(t-1)}\|_2$ was typically observed sooner.

III. MATERIALS AND METHODS

The proposed method was implemented in MATLAB (MathWorks, Natick, MA) for off-line reconstruction on a workstation (Lenovo, Beijing, China) with a 2.66-GHz central processing unit and 8-GB random-access memory.

Written informed consent was obtained from all subjects and the imaging protocol was approved by our Institutional Review Board. All subjects were scanned using a 1.5 T Achieva magnet (Philips Healthcare, Best, NL) with a 5 channel phased-array coil.

A. In Vivo Imaging

Our imaging study was performed for both the left anterior descending (LAD) and the right coronary artery (RCA). Coronary images for right and left coronary MRI was acquired in two different subject cohorts. For each anatomy, 7 healthy adult subject (4 men, 24.4 ± 10.6 years for the RCA; 2 men, 34.7 ± 21.7 years for the LAD) without contraindications to MR imaging were included. Scout images were acquired with a SSFP sequence with 3.12 × 3.12 mm^2 inplane resolution and 10 mm slice thickness. A reference image set was acquired by using the body and phased array coils so that each individual coil sensitivity map could be calculated. This coil map was used only for cine acquisition and was not used in CS reconstruction. This was followed by an image set acquired with an axial breath-hold cine SSFP sequence (TR/TE = 3.7 ms/1.85 ms; temporal resolution, 48 ms; spatial resolution, 1.2 × 1.2 mm^2; acceleration rate, two) to visually identify the quiescent period of the RCA and the LAD. The corresponding trigger delay was used for coronary acquisition. A low-resolution coronary survey three-dimensional (3D) volume was then acquired for localization and assignment of the appropriate imaging slab orientation. A free-breathing 3D electrocardiographically (ECG) gated SSFP sequence (TE/TR = 2.1 ms/4.3 ms; field of view, 270×270×30 mm^3; flip angle, 90°; spatial resolution, 1 × 1 × 3 mm^3) was used to image the RCA and the LAD. A spectrally-selective fat saturation and a T_2 magnetization preparation [6] was used to improve the contrast. A two-dimensional spiral navigator echo, positioned on the right hemi-diaphragm [42], was used for respiratory motion gating with a gating window of 5 mm. The raw k-space data were recorded for all acquisitions. The nominal scan times computed by the scanner for our acquisition parameters and a heart rate of 60 beats per minute are 3 minutes 57 seconds and 3 minutes 43 seconds for the RCA and LAD scans respectively. The actual scan times are higher based on the respiratory gating efficiency, which is usually in the range of 30–50 %.

The k-space data was exported and transferred to a standalone workstation to allow retrospective undersampling by factors of 2, 4, 6, and 8. The central 10 to 16 phase encode lines in the central slices were kept. The edges of the k-space were randomly discarded based on a Gaussian distribution [11], [27]. The choice for the size of central k-space was done experimentally, with a reduced size for higher rates to guarantee enough edge information is included. The relative B_1 coil maps were reconstructed from the fully-sampled data by dividing each individual coil data to the root sum square of all the coil data [21]. As a comparison with the proposed BLS-GSM CS reconstruction, images were also reconstructed using ℓ_1 soft thresholding in IST [17], as well as ℓ_1 minimization via basis pursuit using the SPGL1 [44].

B. Image Analysis

Both subjective and objective image analysis were performed to evaluate the three CS reconstruction at different rates. For each patient, thirteen imaging datasets were reconstructed from the original raw k-space data, which consisted of one from a fully-sampled k-space, 4 datasets reconstructed using BLS-GSM CS for different rates of 2, 4, 6, and 8, 4 datasets using ℓ_1 thresholded CS reconstruction for the same rates, and finally 4 datasets using ℓ_1 minimization for these rates.

The SoapBubble [16] tool was used to quantitatively evaluate the vessel definition utilizing a Deriche algorithm [13] on the RCA. Vessel sharpness scores were calculated for both sides of the vessel. Final normalized sharpness was defined as the average score of both sides normalized by the center of vessel intensity. A sharpness score closer to 1 represents a sharper vessel border.

The mean square error (MSE) of each reconstruction was calculated as

$$\mathrm{MSE}=\sum_{x,y,z}\left|\left|\mathbf{m}_{\mathrm{ref}}(x,y,z)\right|-\left|\mathbf{m}_{\mathrm{reconstructed}}(x,y,z)\right|\right|^{2},$$

where only the magnitude of the reconstructed images were used for comparison to the root-sum-squares reference image. The normalized MSE was then calculated by dividing each individual MSE to the squared ℓ_2 norm of the reference image.

Qualitative assessment of coronary artery image quality was performed by two experienced independent blinded readers with > 10 years coronary MRI experience using a four-point scale system [22]: 1, indicating poor or uninterpretable (coronary artery visible, with markedly blurred borders or edges); 2, good (coronary artery visible, with moderately blurred borders or edges); 3, very good (coronary artery visible, with mildly blurred borders or edges); or 4, excellent (coronary artery visible, with sharply defined borders or edges). For each image, separate scores were given for the proximal, mid and distal segments of RCA for the right coronary scans, and left main, proximal, mid LAD and left circumflex artery (LCX) for the left coronary scans. These scores were combined for the right and left systems respectively for statistical analysis.

C. Statistical Analysis

All measurements are presented as mean ± one standard deviation. Due to the small sample size, and the statistical significance of the Shapiro-Wilk test for normality of the paired differences of the scores (person-specific difference between each technique and the reference which is a fully sampled k-space acquisition), the nonparametric signed rank test was used to test for the null hypothesis that the central tendency of the difference was zero at different acceleration rates. Bonferroni correction was performed to account for multiple comparisons. All statistical analyses were performed using SAS (v9.2, SAS Institute Inc., Cary, NC). A Bonferroni-corrected type-I error of 0.004 (0.05 divided by 12 comparisons) was used to consider for statistical significance.

IV. RESULTS

The top row of Figure 4 shows a sample 2D slice from a 3D right coronary MRI data set reconstructed using ℓ_1 norm thresholding for fully sampled k-space data, and acceleration rates of 4, 6 and 8. The corresponding slice reconstructed using BLS-GSM approach is shown in the middle row, and that for ℓ_1 minimization is shown in the bottom row. RCA can be readily visualized in all images. At higher rates of 6 and 8 the the images reconstructed using ℓ_1 norm thresholding and ℓ_1 minimization suffer from higher level of artifacts. Thus, BLS-GSM allows improved visualization of the coronaries. Figure 5 shows three different

slices from the 3D coronary data set of a different subject reconstucted using BLS-GSM technique for fully sampled k-space data as well as CS acceleration rates of 4, 6 and 8. At acceleration rates of 4 and 6, this approach yield images with image quality comparable to the fully sampled images. There is a degradation of image quality at rate 8, however no distinct visual artifact can be seen. A reduced SNR and increased blurring may impact interpretation of the images even without a distinct artifact at such a high acceleration rate. Figure 6 depicts reformatted images of LAD, LCX and proximal RCA from a 3D left coronary MRI data set reconstructed using the three approaches. The visibility at higher rates are better compared to right coronary data sets, but the degradation at higher rates is still visible. Both ℓ_1 norm approaches suffer from blurring at high rates, although this is manifested differently for each technique. BLS-GSM allows for improved visualization at higher rates, but also has artifacts.

Figure 7 summarizes the imaging scores and MSE of the reconstructed RCA and LAD images using ℓ_1 thresholding, BLS-GSM thresholding, and ℓ_1 minimization. Additionally, sharpness results are included for the RCA. For the RCA, the images reconstructed using BLS-GSM with acceleration rate 8 was scored significantly lower ($p < .0001$) than the fully sampled images. There was no statistically significant difference between acceleration rates of 2 and 6 with BLS-GSM. For ℓ_1 thresholding CS reconstruction, there was significant degradation of image quality for rates 4 and higher, and at rates 6 and higher for ℓ_1 minimization. For the LAD, there was no statistically significant difference between acceleration rates of 2 and 6 with BLS-GSM. Both ℓ_1 -based techniques exhibited significant degradation at rates higher than 4.

The mean value of MSE for BLS-GSM CS was lower than ℓ_1 based techniques for rates 4 and higher for the RCA, with ℓ_1 minimization having a smaller MSE than ℓ_1 thresholding. Similarly, BLS-GSM had the highest sharpness score among the three reconstruction methods. ℓ_1 minimization had a slightly higher sharpness score than ℓ_1 thresholding. For the LAD, the lowest MSE was consistently achieved by ℓ_1 minimization, followed by BLS-GSM CS, and ℓ_1 thresholding.

V. DISCUSSION

We have developed a novel CS reconstruction technique based on exploiting the wavelet domain dependencies of coronary MR images, in addition to wavelet domain sparsity. The reconstruction algorithm alternates between data consistency and thresholding stages. In the thresholding stage, it utilizes a probabilistic model that captures both wavelet domain sparsity and the dependencies of the magnitudes of wavelet domain coefficients in a given neighborhood.

Constraints such as an assumption of deterministic model on the sparsity structure (e.g. assuming the data fits a wavelet-tree model) results in reduction of the the number of measurements required for reconstruction [2]. In our model, we impose a probabilistic model on the sparsity structure using the GSM model, which may allow similar gains, while not limiting the algorithms to a reduced search space containing only signals that fit the proposed model.

There have been several recent works aimed at combining parallel imaging and CS [18], [25], [28]. The proposed approach can be used instead of the conventional ℓ_1 thresholding in the implementation of the CS step of these algorithms. It may also improve image reconstruction in other anatomical or functional imaging, which requires further investigation.

We have chosen the steerable pyramids as the choice of the wavelet transform. However, the GSM model for neighborhoods applies to any wavelet transform. The wavelet dependencies are more pronounced for over-complete or oriented wavelet transforms, such as undecimated discrete wavelet transforms [24], the dual-tree complex wavelet transforms [37] or curvelets [41].

In terms of computational complexity, the data consistency stages complexity is dominated by an FFT and an IFFT, both of $O(n_1 \cdot n_2 \cdot n_3 \cdot \log(n_1 \cdot n_2 \cdot n_3))$, which is standard in many reconstruction algorithms. The thresholding stage for a fixed neighborhood size scales linearly in the transform domain dimensions. However, two numerical integrations are carried out for each wavelet domain coefficient, thus the constant overhead is quite high. On a standard Lenovo workstation with a 2.66-GHz central processing unit and 8-GB random-access memory, the thresholding of a $544 \times 270 \times 18$ volume takes about 5 minutes per iteration using a MATLAB-only implementation. Thus, although the scaling properties of the algorithm are well-behaved, the running time is longer than iterative ℓ_1 methods, but still less than linear programming based methods [7]. Furthermore, the use of overlapping neighborhoods around each central coefficient implies that a given coefficient will be in multiple neighborhoods. Exact global inference on such a model is highly intractable [34], and our sparsity regularizer simply thresholds the central coefficient for each neighborhood separately. Thus, the thresholding no longer corresponds to a MAP estimate. Even though convergence is observed empirically, we do not have a proof of convergence for the IST algorithm with BLS-GSM thresholding.

In our study, we have used a fully sampled data to generate the coil maps, which was used during the reconstruction. In a prospective acquisition, fully-sampled data is not available, therefore a low resolution coil map should be used with proper processing. There are several approaches to better estimate the coil map from low resolution images for parallel imaging reconstruction [21], [35]. These methods could be applied to improve estimation of the coil map for CS reconstruction. Additionally, in coronary MRI, data is acquired only in a short period of cardiac cycle, therefore, a fully sampled data can be acquired with the penalty of potential respiratory motion artifacts in cases where the acquisition window is increased or acquired in different heart phases. The issue of estimating the optimal coil map was not studied and requires further investigation, especially in an iterative reconstruction where errors of estimation can easily propagate through reconstruction steps.

Our study has limitations. Only a small number of young healthy adult subjects were studied. Further studies are needed to study the clinical evaluation of the proposed coronary MRI for diagnosis of coronary artery disease. We have also not compared our method to total variation based methods. Additionally, all undersampling experiments were performed retrospectively. This study used a retrospective approach as the first step to evaluate the

feasibility of CS in coronary MRI. Therefore the achievable acceleration rates in a prospective study might be lower. Furthermore, other factors such as optimal undersampling pattern, eddy current due to random jumps in k-space, optimal phase ordering scheme, considering its impact on contrast and signal to noise ratio as well as flow, needs to be fully investigated prior to a prospective acquisition. The choice of neighborhood size was determined experimentally, and was fixed for the duration of the study. The choice of thresholding parameter was not automated and was selected empirically.

VI. CONCLUSION

We have developed and evaluated an improved CS reconstruction method for accelerating coronary MRI by exploiting the dependencies of the wavelet coefficients in addition to their sparsity.

Acknowledgments

The authors would like to thank Kraig V. Kissinger, Beth Goddu and Lois A. Goepfert for their help with MRI scans, and Alan O'Connor for insightful discussions.

The project described was supported by NIH R01EB008743-01A2, AHA SDH-0730339N and NIH UL1 RR025758-01, Harvard Clinical and Translational Science Center, from the National Center for Research Resources.

APPENDIX A: SPARSITY MODELING WITH JEFFREY'S PRIOR

Consider the sparsity model, where each transform domain coefficient is assumed to be i.i.d., i.e. the GSM neighborhoods are one-dimensional. Since orientation and scale are not important in this discussion, we will index the wavelet coefficients as $\{u_k\}$ for ease of notation, where k indexes through the whole wavelet space. With $p_z(z) = 1/z$, the single-wavelet-domain-voxel probability density function in the GSM model *is* $p_x(x) = p_u(u) \propto 1/|u|$ [36]. In the Bayesian interpretation, this corresponds to a regularizer $\Phi(\mathbf{m}) = \sum_k \log|u_k|$. There is a one-to-one correspondence between the minimizer of Equation (1) with this regularizer and the sparsity regularizer based on ℓ_0-norm $\| \mathbf{u} \|_0$, since

$\|\mathbf{u}\|_0 = lim_{p\to 0} \sum_k |u_k|^p$ and $\lim_{p\to 0} \frac{1}{p}(\sum_k |u_k|^p - 1) = \sum_k \log|u_k|$ [45]. Thus Jeffrey's prior (with i.i.d. transform domain coefficients) models sparsity regularization with ℓ_p norm minimization where $p \to 0$.

APPENDIX B: STUDY OF NOISE RESILIENCE

In order to assess the immunity of proposed method against a range of noise variance levels, the following study was carried out: A 2D MRI scan of a resolution phantom, with a spatial resolution of 1×1 mm^2 was performed. A reference image was generated from this data using root-sum-squares of each coil image. The SNR of this image was measured, as the ratio of the signal intensity in a prescribed region-of-interest (ROI), and the signal standard deviation in a region of noise-only signal. This SNR was subsequently used as the baseline SNR. Then Gaussian noise was added to the original k-space data, and another image was generated. The relative SNR (rSNR) was defined as the ratio of the SNR of this image to the

the baseline SNR. The noisy k-space data were then undersampled at an acceleration rate of four, and reconstructed using the proposed technique. The normalized MSE (with respect to the reference) were measured for each reconstruction, as well as for the noisy image generated from the full noisy k-space data. The results are depicted in Figure 8.

The results indicate that the MSE of BLS-GSM increases with noise. The scaling is roughly linear with the square of the noise magnitude (or inverse square of the rSNR), as predicted by the CS theory. We note that at very low rSNR, the reconstructed image has a lower MSE than the image generated from the fully-sampled noisy k-space, due to the thresholding abilities of the algorithm.

References

1. Andrews D, Mallows C. Scale mixtures of normal distributions. J R Stat Soc. 1974; 36:99–102.
2. Baraniuk R, Cevher V, Duarte M, Hegde C. Model-based compressive sensing. IEEE Trans on Inf Theory. Apr; 2010 56(4):1982–2001.
3. Bhat H, Yang Q, Zuehlsdorff S, Li K, Li D. Contrast-Enhanced Whole-Heart Coronary Magnetic Resonance Angiography at 3 T Using Interleaved Echo Planar Imaging. Investigative Radioloogy. 2010 in press.
4. Bi X, Carr JC, Li D. Whole-heart coronary magnetic resonance angiography at 3 Tesla in 5 minutes with slow infusion of Gd-BOPTA, a high-relaxivity clinical contrast agent. Magnetic Resonance in Medicine. 2007; 58(1):1–7. [PubMed: 17659628]
5. Block KT, Uecker M, Frahm J. Undersampled radial MRI with multiple coils. Iterative image reconstruction using a total variation constraint. Magnetic Resonance in Medicine. 2007; 57(6): 1086–1098. [PubMed: 17534903]
6. Brittain JH, Hu BS, Wright GA, Meyer CH, Macovski A, Nishimura DG. Coronary angiography with magnetization-prepared T_2 contrast. Magnetic Resonance in Medicine. 1995; 33(5):689–696. [PubMed: 7596274]
7. Candès EJ, Romberg J, Tao T. Robust uncertainty principles: exact signal reconstruction from highly incomplete frequency information. IEEE Trans on Inf Theory. Feb; 2006 52(2):489–509.
8. Chartrand R. Exact reconstructions of sparse signals via nonconvex minimization. IEEE Signal Proc Letters. 2007; 14(10):707–710.
9. Chartrand, R. Proceedings of IEEE International Symposium on Biomedical Imaging. Boston, MA: Jun. 2009 Fast algorithms for nonconvex compressive sensing: MRI reconstruction from very few data.
10. Combettes PL, Wajs VR. Signal recovery by proximal forward-backward splitting. SIAM Journal on Multiscale Modeling and Simulation. Nov.2005 4:1168–1200.
11. Çukur T, Lustig M, Nishimura DG. Improving non-contrast-enhanced steady-state free precession angiography with compressed sensing. Magnetic Resonance in Medicine. 2009; 61(5):1122–1131. [PubMed: 19230013]
12. Daubechies I, Defries M, De Mol C. An iterative thresholding algorithm for linear inverse problems with a sparsity constraint. Communications on Pure and Applied Mathematics, vol. 2004; 57:1413–1457.
13. Deriche R. Fast algorithms for low-level vision. IEEE Trans on Pattern Anal Mach Intell. 1990; 12:78–87.
14. Donoho DL. Compressed Sensing. IEEE Trans on Inf Theory. Apr; 2006 52(4):1289–1306.
15. Donoho D, Johnstone I. Ideal adaptation via wavelet shrinkage. Biometrika. 1994; 81:425–455.
16. Etienne A, Botnar RM, Van Muiswinkel AM, Boesiger P, Manning WJ, Stuber M. ‘Soap-Bubble’ visualization and quantitative analysis of 3D coronary magnetic resonance angiograms. Magnetic Resonance in Medicine. 2002; 48:658–666. [PubMed: 12353283]
17. Figueiredo M, Nowak R. An EM algorithm for wavelet-based image restoration. IEEE Trans Image Proc. Aug.2003 12:906–916.

18. Fischer, A.; Seiberlich, N.; Blaimer, M.; Jakob, PM.; Breuer, FA.; Griswold, MA. A Combination of Nonconvex Compressed Sensing and GRAPPA (CS-GRAPPA). Proceedings 17th Scientific Meeting, International Society for Magnetic Resonance in Medicine; Honolulu. April 2009;
19. Gamper U, Boesiger P, Kozerke S. Compressed sensing in dynamic MRI. Magnetic Resonance in Medicine. 2008; 59(2):365–373. [PubMed: 18228595]
20. Huber ME, Kozerke S, Pruessmann KP, Smink J, Boesiger P. Sensitivity-encoded coronary MRA at 3T. Magnetic Resonance in Medicine. 2004; 52(2):221–227. [PubMed: 15282803]
21. Kellman P, Epstein FH, McVeigh ER. Adaptive sensitivity encoding incorporating temporal filtering (TSENSE). Magnetic Resonance in Medicine. 2001; 45:846–852. [PubMed: 11323811]
22. Kim WY, Danias PG, Stuber M, Flamm SD, Plein S, Nagel E, Langerak SE, Weber OM, Pedersen EM, Schmidt M, Botnar RM, Manning WJ. Coronary magnetic resonance angiography for the detection of coronary stenoses. New England Journal of Medicine. 2001; 345(26):1863–1869. [PubMed: 11756576]
23. Kim YC, Narayanan SS, Nayak KS. Accelerated three-dimensional upper airway MRI using compressed sensing. Magnetic Resonance in Medicine. 2009; 61(6):1434–1440. [PubMed: 19353675]
24. Lang M, Guo H, Odegard JE, Burrus CS, Wells RO Jr. Nonlinear processing of a shift-invariant discrete wavelet transform (DWT) for noise reduction. Proc SPIE. 1995; 2491:640.
25. Liang, D.; King, K.; Liu, B.; Ying, L. Accelerating SENSE using distributed compressed sensing. Proceedings 17th Scientific Meeting, International Society for Magnetic Resonance in Medicine; Honolulu. April 2009;
26. Lloyd-Jones D, Adams RJ, Brown TM, Carnethon M, Dai S, De Simone G, Ferguson TB, Ford E, Furie K, Gillespie C, Go A, Greenlund K, Haase N, Hailpern S, Ho PM, Howard V, Kissela B, Kittner S, Lackland D, Lisabeth L, Marelli A, McDermott MM, Meigs J, Mozaffarian D, Mussolinom M, Nichol G, Roger V, Rosamond W, Sacco R, Sorlie P, Stafford R, Thom T, Wasserthiel-Smoller S, Wong ND, Wylie-Rosett J. Heart Disease and Stroke Statistics–2010 Update. A Report From the American Heart Association. Circulation. 2009
27. Lustig M, Donoho DL, Pauly JM. Sparse MRI: The application of compressed sensing for rapid MR imaging. Magnetic Resonance in Medicine. 2007; 58(6):1182–1195. [PubMed: 17969013]
28. Lustig, M.; Alley, M.; Vasanawala, S.; Donoho, DL.; Pauly, JM. L1 SPIR-iT: Autocalibrating Parallel Imaging Compressed Sensing. Proceedings 17th Scientific Meeting, International Society for Magnetic Resonance in Medicine; Honolulu. April 2009;
29. Meyer CH, Hu BS, Nishimura DG, Macovski A. Fast spiral coronary artery imaging. Magnetic Resonance in Medicine. 1992; 28:202–213. [PubMed: 1461123]
30. Nayak KS, Pauly JM, Yang PC, Hu BS, Meyer CH, Nishimura DG. Real-time interactive coronary MRA. Magnetic Resonance in Medicine. 2001; 46(3):430–435. [PubMed: 11550232]
31. Niendorf T, Hardy CJ, Giaquinto RO, Gross P, Cline HE, Zhu Y, Kenwood G, Cohen S, Grant AK, Joshi S, Rofsky NM, Sodickson DK. Toward single breath-hold whole-heart coverage coronary MRA using highly accelerated parallel imaging with a 32-channel MR system. Magnetic Resonance in Medicine. 2006; 56(1):167–176. [PubMed: 16755538]
32. Niendorf T, Saranathan M, Lingamneni A, Pedrosa I, Spencer M, Cline H, Foo TKF, Rofsky NM. Short breath-hold, volumetric coronary MR angiography employing steady-state free precession in conjunction with parallel imaging. Magnetic Resonance in Medicine. 2005; 53:885–894. [PubMed: 15799036]
33. Otazo, R.; Xu, J.; Kim, D.; Axel, L.; Sodickson, DK. Combination of Compressed Sensing and Parallel Imaging for Highly-Accelerated 3D First-Pass Cardiac Perfusion MRI. Proceedings 18th Scientific Meeting, International Society for Magnetic Resonance in Medicine; Stockholm, Sweden. May 2010;
34. Portilla J, Strela V, Wainwright MJ, Simoncelli EP. Image Denoising Using Scale Mixtures of Gaussians in the Wavelet Domain. IEEE Trans Image Proc. Nov.2003 12:1338–1351.
35. Pruessmann K, Weiger M, Scheidegger M, Boesiger P. SENSE: sensitivity encoding for fast MRI. Magnetic Resonance in Medicine. 1999; 42:952–962. [PubMed: 10542355]
36. Robert, C. The Bayesian Choice: A Decision Theoretic Motivation. First. New York, NY: Springer-Verlag; 1994.

37. Selesnick IW, Baraniuk RG, Kingsbury NG. The dual-tree complex wavelet transform – A coherent framework for multiscale signal and image processing. IEEE Signal Processing Magazine. Nov; 2005 22(6):123–151.
38. Shapiro J. Embedded image coding using zerotrees of wavelet coefficients. IEEE Trans Signal Processing. Dec.1993 41:3445–3462.
39. Simoncelli EP, Freeman WT, Adelson EH, Heeger DJ. Shiftable multi-scale transforms. IEEE Trans Inf Theory. Mar.1992 38:587–607.
40. Sodickson DK, Manning WJ. Simultaneous acquisition of spatial harmonics (SMASH): Fast imaging with radiofrequency coil arrays. Magnetic Resonance in Medicine. 1997; 38:591–603. [PubMed: 9324327]
41. Starck J, Candès EJ, Donoho DL. The curvelet transform for image denoising. IEEE Trans Image Processing. Jun.2002 11:670–684.
42. Stuber M, Botnar RM, Danias PG, Sodickson DK, Kissinger KV, Van Cauteren M, De Becker J, Manning WJ. Double-oblique free-breathing high resolution three-dimensional coronary magnetic resonance angiography. Journal of the American College of Cardiology. 1999; 34(2):524–531. [PubMed: 10440168]
43. Trzasko J, Manduca A, Borisch E. Highly undersampled magnetic resonance image reconstruction via homotopic ℓ_0-minimization. IEEE Trans Medical Imaging. Jan; 2009 28(1):106–121.
44. van den Berg E, Friedlander MP. Probing the Pareto frontier for basis pursuit solutions. SIAM Journal on Scientific Computing. 2008; 31(2):890–912.
45. Wipf DP, Nagarajan S. Iterative Reweighted ℓ_1 and ℓ_2 Methods for Finding Sparse Solutions. IEEE Journal of Selected Topics in Signal Processing. Apr; 2010 4(2):317–329.

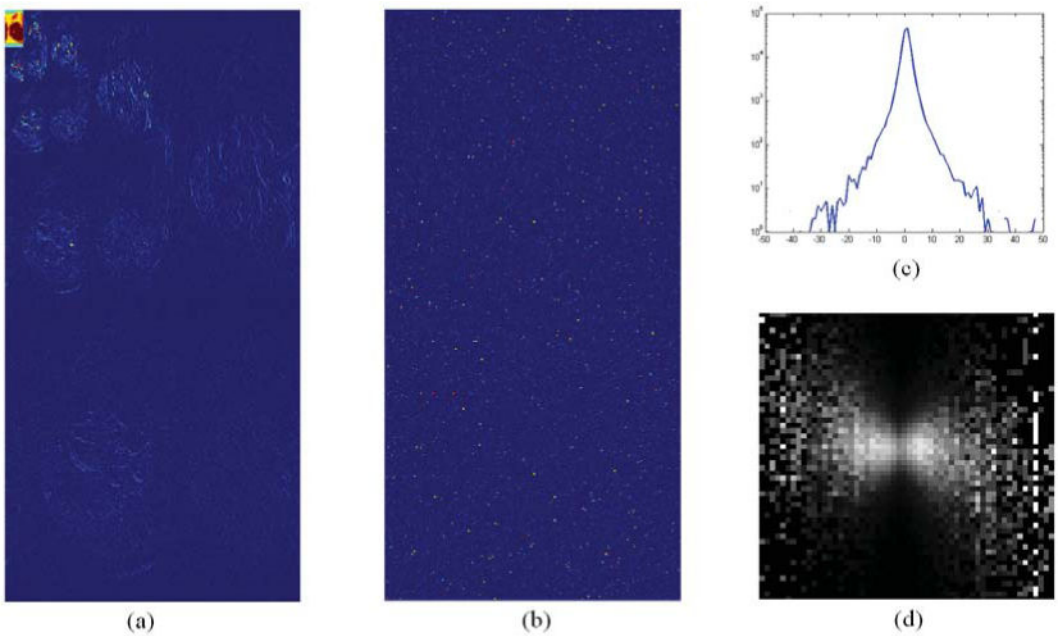

Fig. 1.

(a) Wavelet coefficients (Haar) of a 2D slice of a coronary image (blue = 0). (b) Random permutation of the same coefficients shown in (a). Both data have equivalent ℓ_p norm, which suggests ℓ_p norm regularizes do not take into account the clustering and correlation of information in the wavelet domain, as exhibited in (a). (c) shows the log marginal histogram of wavelet coefficients from one subband (magnitude image), and (d) shows the conditional histogram for two adjacent wavelet coefficients. The empirical distributions have similar characteristics as the Gaussian Scale Mixture model.

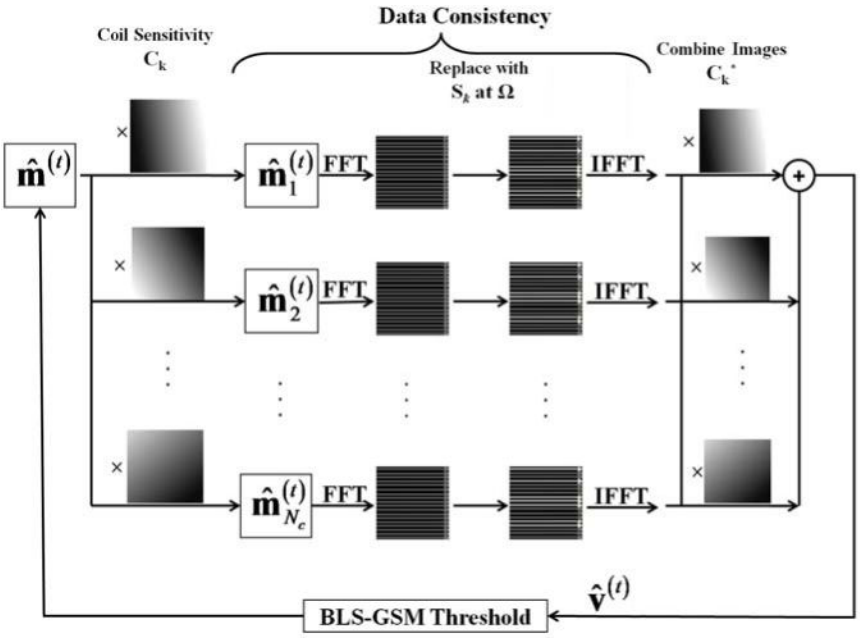

Fig. 2.

The proposed reconstruction algorithm for coronary MRI. In the data consistency stage, the acquired k-space lines replaces the corresponding k-space lines of the estimate. In the thresholding stage, we use our proposed Bayesian Least Squares – Gaussian Scale Mixture (BLS-GSM) thresholding, instead of conventional ℓ_1 soft thresholding strategy. We note that the sampling pattern depicted here is a simple example for visualization purposes, and the actual 3D undersampling patterns are described in Section III-A.

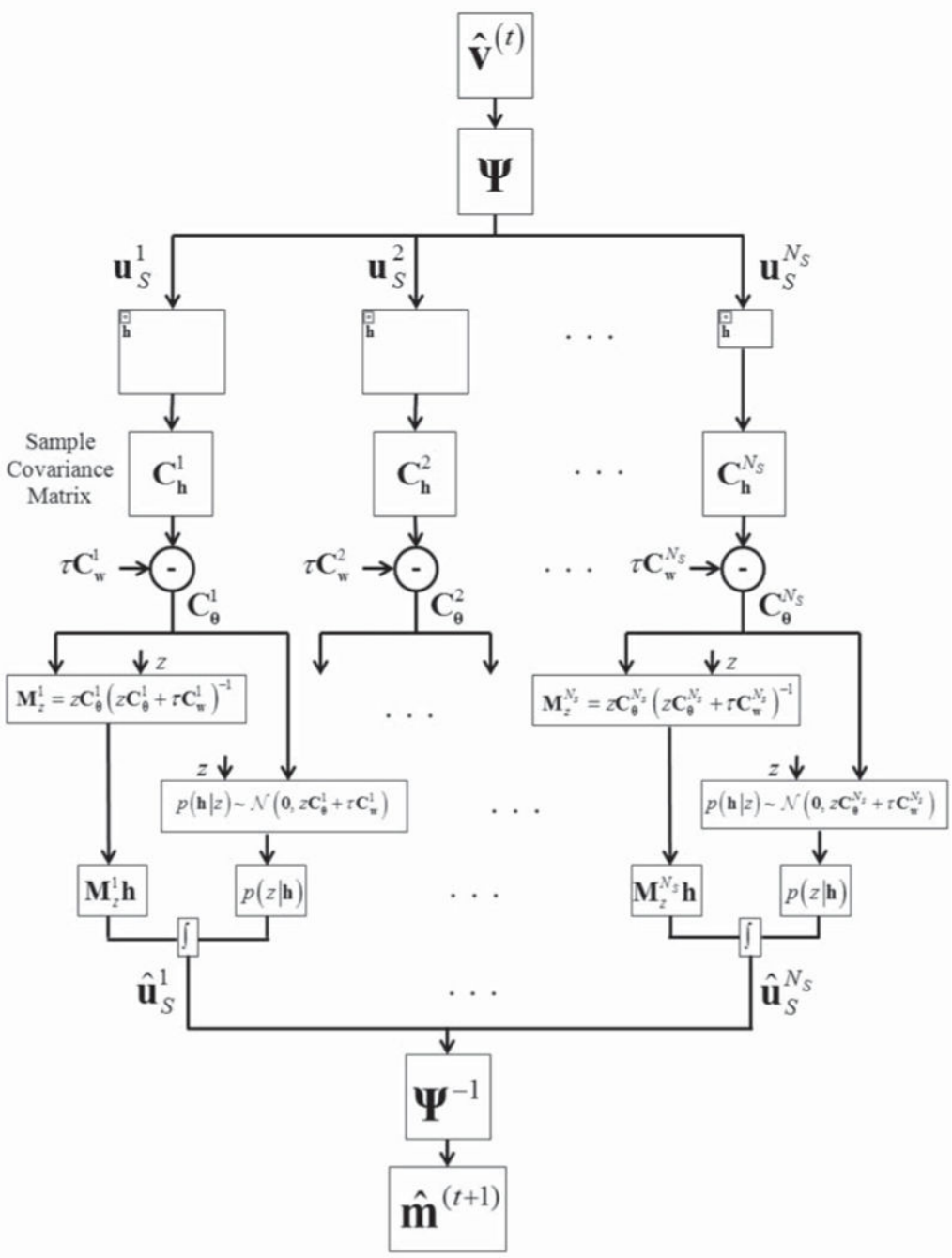

Fig. 3.

The proposed BLS-GSM thresholding algorithm for coronary MRI. For each of the N_S subbands of the wavelet transform, the sample covariance matrix of the current image estimate, $\mathbf{C}_\mathbf{h}^k$ is calculated over neighborhoods $\mathbf{h}$. Using the pre-computed sample noise covariance matrix of the same subband, the neighborhood covariance is calculated by keeping the positive semi-definite part of the noise-adjusted covariance matrix $\mathbf{C}_\theta^k = (\mathbf{C}_\mathbf{h}^k - \tau\mathbf{C}_\mathbf{w}^k)_+$. Using these covariance matrices, the Wiener estimate of each

neighborhood of the subband is calculated by $z\mathbf{C}_{\boldsymbol{\theta}}^{\boldsymbol{k}}(z\mathbf{C}_{\boldsymbol{\theta}}^{\boldsymbol{k}}+\tau\mathbf{C}_{\mathbf{w}}^{\boldsymbol{k}})^{-1}\mathbf{h}$ for every z in the integration range. The probability density function $p(z|\mathbf{h})$ for the subband is also calculated for the integration range of z via Bayes' rule. The thresholded estimate for each coefficient in the subband is then calculated by numerical integration with respect to z of the corresponding coefficient of the Wiener estimate multiplied by $p(z|\mathbf{h})$.

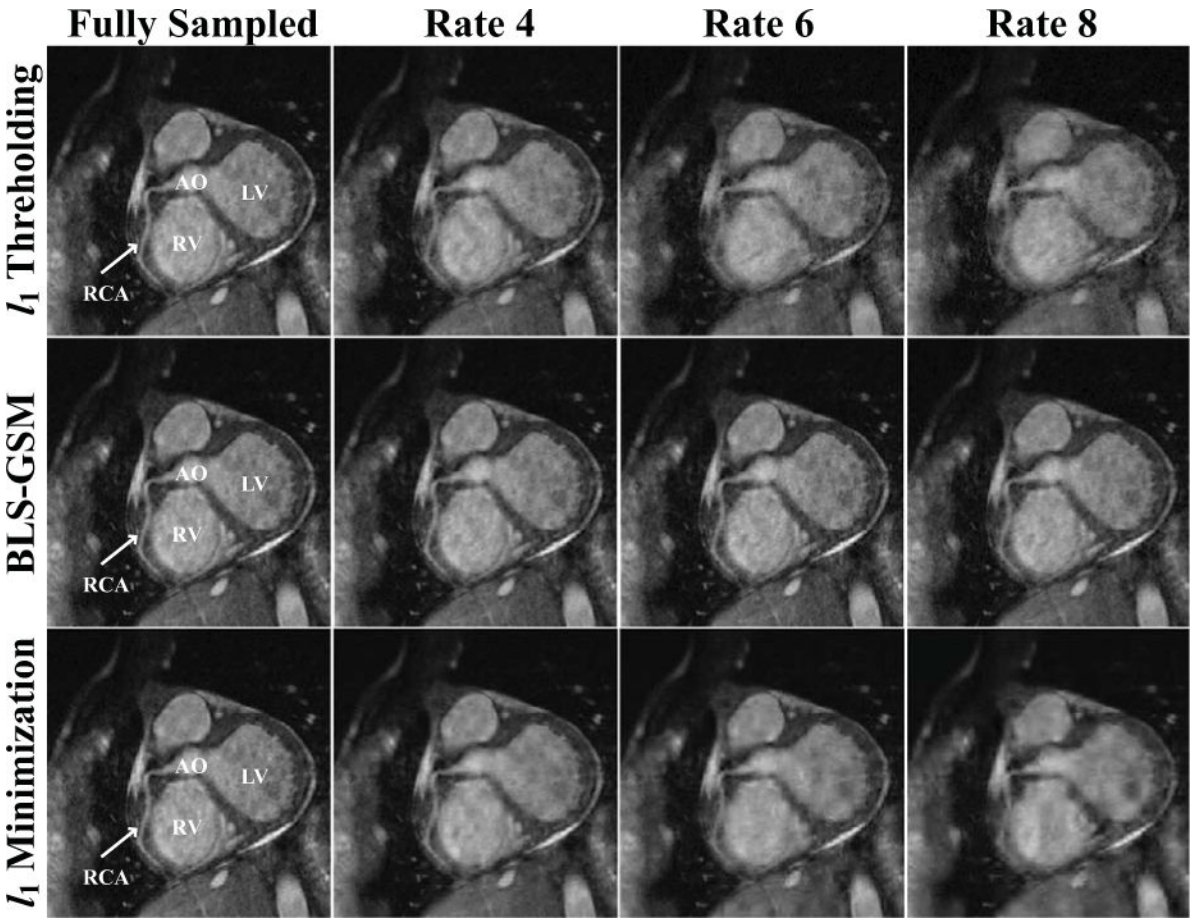

Fig. 4.

An example slice of a 3D right coronary MR image from fully-sampled data (reference), and from ℓ_1 thresholded (top row), BLS-GSM thresholded (middle row) and ℓ_1 minimized (bottom row) reconstructions for accelerated acquisition rates of 4, 6 and 8. Right coronary artery (RCA) can be readily visualized in all images, although more artifacts are visible at higher rates and for ℓ_1 norm-regularized CS (AO: Aortic Root, RV: Right Ventricle, LV: Left Ventricle).

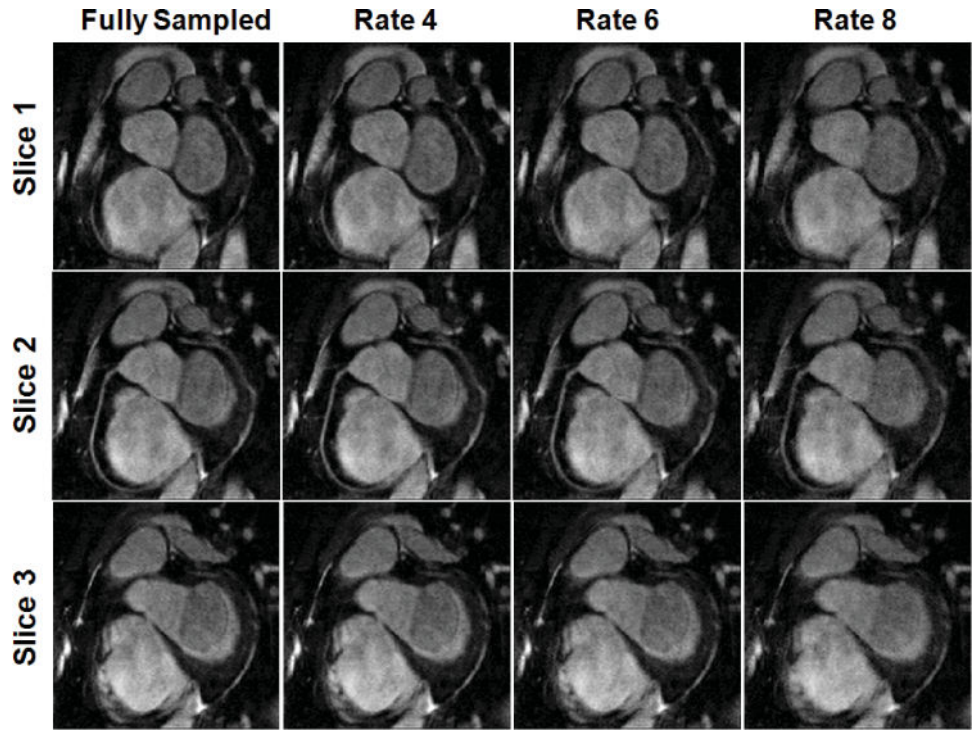

Fig. 5.

Multiple slices of a 3D coronary MR image from fully-sampled data (reference), and from reconstructions using the proposed BLS-GSM method for accelerated acquisition rates of 4, 6 and 8.

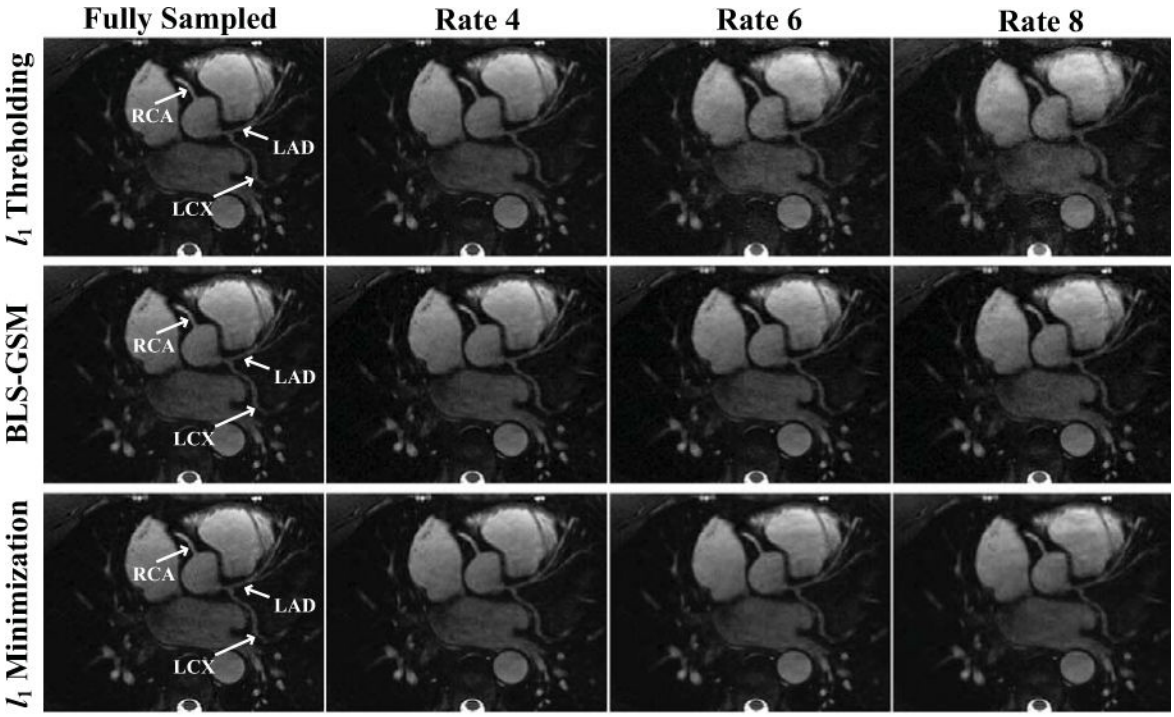

Fig. 6.

Reformatted axial images of right coronary artery (RCA), left anterior descending artery (LAD) and left circumflex artery (LCX) from fully-sampled 3D left coronary MRI data (reference), and from ℓ_1 thresholded (top row), BLS-GSM thresholded (middle row) and ℓ_1 minimized (bottom row) reconstructions for accelerated acquisition rates of 4, 6 and 8. The coronaries can be readily visualized in all images, although blurring is apparent at higher rates for ℓ_1 norm-regularized CS.

			BLS-GSM Thresholding CS				l_1 Thresholding CS				l_1 Minimization CS			
		REF	R2	R4	R6	R8	R2	R4	R6	R8	R2	R4	R6	R8
RCA	score	3.2 ± 0.9	3.1 ± 1.0	3.0 ± 1.0	2.9 ± 1.0	2.8 ± 0.9	3.2 ± 1.0	2.7 ± 0.9	2.1 ± 0.8	1.8 ± 0.7	3.2 ± 1.0	2.9 ± 0.9	2.5 ± 0.9	2.0 ± 0.7
	P-value	NA	1.0000	0.0574	0.0247	<.0001	0.5488	<.0001	<.0001	<.0001	0.5488	0.0394	<.0001	<.0001
	MSE (norm.)	NA	0.001 ± 0.002	0.003 ± 0.005	0.007 ± 0.006	0.016 ± 0.007	0.000 ± 0.001	0.005 ± 0.004	0.021 ± 0.005	0.036 ± 0.010	0.000 ± 0.001	0.004 ± 0.001	0.010 ± 0.004	0.016 ± 0.003
	Sharpness (norm.)	0.497 ± 0.084	0.485 ± 0.091	0.471 ± 0.084	0.464 ± 0.077	0.400 ± 0.081	0.493 ± 0.090	0.448 ± 0.083	0.409 ± 0.101	0.373 ± 0.114	0.493 ± 0.090	0.438 ± 0.088	0.413 ± 0.081	0.375 ± 0.076
LAD / LCX	score	3.0 ± 0.8	3.1 ± 0.9	3.0 ± 0.8	2.9 ± 0.9	2.7 ± 0.9	3.0 ± 0.9	2.9 ± 0.9	2.1 ± 0.6	1.9 ± 0.6	3.0 ± 0.9	2.8 ± 0.9	2.5 ± 0.8	2.0 ± 0.6
	P-value	NA	0.5488	0.7744	0.3593	0.0002	1.0000	0.2379	<.0001	<.0001	1.0000	0.0071	<.0001	<.0001
	MSE (norm.)	NA	0.006 ± 0.004	0.009 ± 0.005	0.013 ± 0.006	0.023 ± 0.007	0.000 ± 0.001	0.003 ± 0.001	0.026 ± 0.004	0.053 ± 0.009	0.001 ± 0.000	0.003 ± 0.002	0.008 ± 0.001	0.015 ± 0.002

Fig. 7.

The imaging score and associated *p*-value, normalized mean square error (MSE) and normalized sharpness for all reconstruction rates using BLS-GSM thresholding, ℓ_1 thresholding, and ℓ_1 minimization.

Relative SNR	1	0.5	0.2	0.1	0.05	0.02	0.01
MSE (BLS-GSM Recon)	0.063	0.086	0.098	0.100	0.129	0.206	0.292
MSE (Noisy Image)	0.000	0.006	0.027	0.059	0.109	0.322	0.581

Fig. 8.

The results of the artificial noise study. The MSE of BLS-GSM reconstructions increase with noise, but stays bounded. At lower relative SNRs, the thresholding allows for partial noise removal.